Strojniški vestnik - Journal of Mechanical Engineering 69(2023)1-2, 17-31
DOI:10.5545/sv-jme.2022.427
Original Scientific Paper
Received for review: 2022-10-27
Received revised form: 2022-12-30
Accepted for publication: 2023-01-09
© 2023 The Authors. CC BY-NC 4.0 Int. Licensee: SV-JME

Analysis of the Dynamic Characteristics of a Gear-Rotor-Bearing System with External Excitation

Risu Na – Kaifa Jia* – Shujing Miao – Weiguo Zhang – Quan Zhang
Inner Mongolia University of Technology, College of Mechanical Engineering, China

The dynamic response of the rotor system in a ring die granulator is complex and difficult to solve when it operates under joint external, support and gear mesh forces. To solve this problem, a finite element method and extrusion theory was applied in this study to develop a dynamic coupling model for a hollow overhung rotor with external load excitation. A Newmark-β numerical integration method was used to solve for the dynamic response of the overhung rotor under multiple excitation forces. The results included time-domain response diagrams, frequency-domain response diagrams, phase diagrams, Poincaré section diagrams, and bifurcation diagrams. The model and the method were verified by testing a ring die granulator. On this basis, the dynamic response of the system is predicted according to the influence of different parameters. As the bearing support distance increased, the roller eccentricity decreased, the bearing clearance decreased, the response of the rotor system was significantly optimized, and the system tended to stabilize gradually. Therefore, this paper provides a theoretical basis and experimental verification for the optimization of a pelleting machine transmission structure.
Keywords: rotor dynamics, external incentives, finite element method, bearing, gear

Highlights
- *Bearing clearance will affect the internal excitation of the bearing support of the system, so the influence law of different clearance parameters on the system is discussed.*
- *The clearance of a helical gear can affect the internal excitation of the system-bearing support, so the influence law of different clearance parameters on the system is discussed.*
- *Bearing support distance will affect the dynamic response of the system, so the influence law of different support distance parameters on the system is discussed.*
- *The external load model of a ring mold pelleting machine is established, and its dynamic characteristics are explored according to the important parameters of production and operation.*
- *The accuracy and correctness of the theoretical calculation are verified with experiments.*

0 INTRODUCTION

Ring die granulators are key components used in the granulation processing. They are not only used in the feed-processing industry but are also widely used in emerging biomass pellet fuel molding industries. The dynamic response of the rotor is complex, making it difficult to calculate and predict. The rotor system in a ring die granulator is prone to rotor instability due to the combination of the gear mesh force, the bearing support force, and the external load force. However, studies regarding the responses of rotor systems experiencing random extrusion external loads are rarely reported. To improve the stability of this type of rotor and the service life of its key components, the dynamic response of a hollow overhung rotor experiencing multiple external forces was investigated in this study, and the effect patterns of the key parameters were explored.

Schwarz et al. [1] and other research groups [2] to [3] used dynamic simulations and machine learning algorithms to study the impact of highly dynamic cage motion on the performance of rolling bearings. Smagala and Kecik [4] and Kurvinen et al. [5] used a two-degree-of-freedom nonlinear bearing model and the Hertz theory to study the effects of the number of balls and the rotational speed of the rotating axle on the dynamic response. Many scholars [6] to [9] have carried out extensive research on bearing failure dynamics and other aspects, and the results provide help for the ontology.

Chen et al. [10] proposed a dynamic model of spur gear with straight teeth, which takes into account the detailed deformation of a single tooth, including the flexible deformation of the tooth surface, the deformation of the tooth body, the contact deflection of the local tooth surface and the deformation due to its neighbouring loaded teeth. Zheng et al. [11] and Zhu et al. [12] focused on the centrifugal force in high-speed working conditions, developed an analytical finite element method (FEM) framework to integrate the centrifugal field into the mesh stiffness and nonlinear dynamics. Shi and Li [13] proposed a dynamics model for hypoid gears, considering mesh stiffness that is dependent on dynamic mesh force. Based on the spectral density of excitation and the frequency response function of the transfer path between the excitation point and measurement point, Hajnayeb

*Corr. Author's Address: Inner Mongolia University of Technology, College of Mechanical Engineering, China, 1642523516@qq.com

and Sun [14] proposed a new method to determine the influence of random manufacturing errors on vibration measurement on mating gear bearings. In the work of Liu et al. [15], mesh characteristics of the spur gear paired with the pitch deviation are studied in order to analyse the time-varying contact ratio and motion characteristics of the system. Xu et al. [16] used a loaded tooth contact analysis method and conducted quasi-static experiments to determine the coefficient matrix describing the relationship between the mesh force and the strain. Cirelli et al. [17] and [18] proposed an improved method to simulate the nonlinear dynamic response of spur gears. Mo et al. [19] and [20] discussed the effects of flexible support stiffness and floating components on the stability and reliability of a herringbone planetary gear system. Other researchers proposed a variety of accurate and effective time-varying mesh stiffness calculation methods, including the potential energy method, and discussed the effects of temperature and shock on the mesh stiffness [21] to [23]. In comparison, the calculation model of gear meshing stiffness and meshing error based on Fourier series is more widely used because of its representativeness.

Other researchers [24] to [27] proposed a Timoshenko beam consisting of a chain of masses and straight segments, accounting for the bending and shear deformations of the linear rotational and transverse springs. Zhan et al. [28] and Si et al. [29] studied the free vibrations of axially-loaded multi-cracked Timoshenko beams with different boundary conditions, such as hinged, cramped, clamped-hinged, and cramped-free. Based on the Timoshenko beam theory and using Hamilton's principle and Euler angles, Zhu et al. [30] and Zhang et al. [31] developed a novel mathematical model for a rotating axle with an efficient centrifugal term. The solution of rotor dynamic response based on discrete elements can not only deal with the influence of complex excitations but also has s high solving accuracy.

An extrusion mechanics model for a ring die was constructed as a function of vibration. Using a nonlinear deep groove ball bearing support mechanics model and a helical gear mesh mechanics model, the dynamic characteristics of the overhung rotor of a ring die granulator were analysed and used as a case study. The accuracy and validity of the theoretical model for coupled rotor dynamics were verified with experiments. This method takes into account the effects of complex load coupling and can provide guidance for solving and optimizing the dynamic response of irregular rotors.

1 COUPLED ROTOR MODEL WITH EXTERNAL EXCITATION

A ring die granulator rotor system consists of a hollow axle, a ring die, a gear, and a bearing, as shown in Fig. 1. Rotor vibration is an important cause of declining granulation efficiency and granulation quality. Multiple acting forces are significant factors affecting the stability of the rotor system. To improve the calculation efficiency and accuracy, the hoop-locking connection between the ring die and the hollow axle was simplified as a rigid connection, with the assumption that the material of the rotating axle was uniform, and the keyway and the chamfering effects were negligible. A system dynamics model was developed using the Timoshenko finite element analysis method and the lumped mass method. The differential principle was used to discretize the variable-segment rotor and to divide the rotor system into 20 axle segments and 21 nodes as shown in Fig. 2.

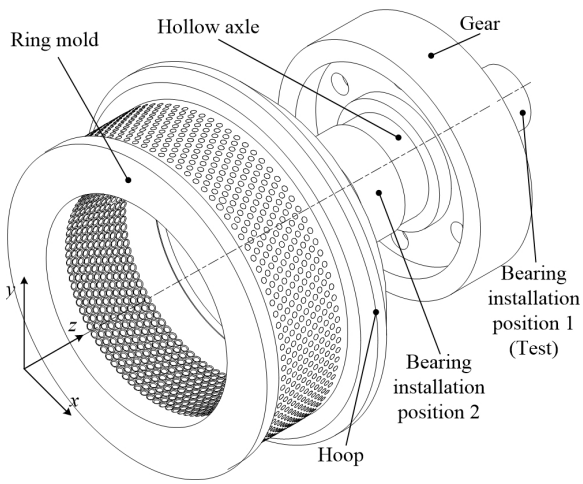

Fig. 1. *Drive rotor system of ring mold granulator*

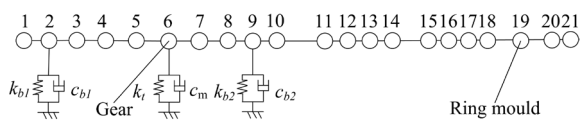

Fig. 2. *Finite element model of ring mold granulator rotor*

According to the rotor structure of the ring die granulator, the finite element rotor model with the radial translational displacement and bending displacement vectors contained displacement vectors for a total of 84 element nodes. The element displacement vector for each axle segment could be expressed by Eq. (1). The supporting forces for the left and right bearings, the mesh force of the helical gear, and the pressing force of the ring die acted

on the second, ninth, sixth, and nineteenth nodes, respectively.

$$\mathbf{u}_{\mathbf{si}} = \left[x_{\mathrm{A}}, y_{\mathrm{A}}, \theta_{x\mathrm{A}}, \theta_{y\mathrm{A}}, x_{\mathrm{B}}, y_{\mathrm{B}}, \theta_{x\mathrm{B}}, \theta_{y\mathrm{B}} \right]^{\mathrm{T}}. \quad (1)$$

In Eq. (1), x_{A} and y_{A} represent the x and y radial vibration displacements of the centre at the left end face, A, of the axle segment, respectively. $\theta_{x\mathrm{A}}$ and $\theta_{y\mathrm{A}}$ represent the radial angular displacements of the centre at the left end face, A, respectively. In a similar way, the displacements of the right end face, B, could be obtained. $\mathbf{u}_{\mathbf{si}}$ represents the i^{th} element displacement vector of the rotor. The mass matrix, $\mathbf{M}_{\mathbf{si}}$, the stiffness matrix, $\mathbf{K}_{\mathbf{si}}$, the gyro matrix, $\mathbf{G}_{\mathbf{si}}$, and the external force matrix, $\mathbf{F}_{\mathbf{si}}$, could be obtained for the i^{th} element. The element matrices were assembled as shown in Fig. 3, and the rotor system's global mass matrix, **M**, global stiffness matrix, **K**, global gyro matrix, **G**, and global external force matrix, **F**, were obtained.

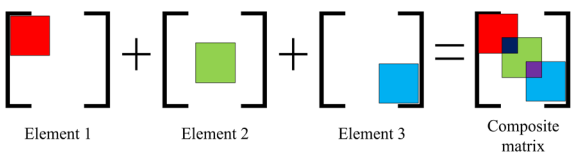

Fig. 3. *Timoshenko beam element matrix assembly*

By using Rayleigh damping to calculate the rotor viscous damping, matrix **C** could be expressed by Eq. (2):

$$\mathbf{C} = \alpha_{\mathrm{o}}\mathbf{M} + \beta_{\mathrm{o}}\mathbf{K}, \quad (2)$$

where α_{o} and β_{o} are the proportional Rayleigh damping coefficients. The nodal displacement vector of the rotor system can be expressed by $\mathbf{X} = [x_1\ x_2\ \cdots\ x_{84}]$.

According to the energy method, the dynamic equation for the overhung hollow rotor with multi-force coupling in the ring die granulator was established as Eq. (3):

$$\mathbf{M}\ddot{\mathbf{X}} + (\mathbf{C} + \omega\mathbf{G})\dot{\mathbf{X}} + \mathbf{K}\mathbf{X} = \mathbf{Q}. \quad (3)$$

In Eq. (3), **Q** represents the assembled external force matrix for the coupled rotor system, which includes the gear mesh force matrix, $\mathbf{F}_{\mathbf{g}}$, the bearing support force matrix, $\mathbf{F}_{\mathbf{b}}$, the ring die extrusion force matrix, $\mathbf{F}_{\mathbf{h}}$, and the axle external force matrix, **F**, $\ddot{\mathbf{X}}$, $\dot{\mathbf{X}}$, and **X** are the acceleration, velocity, and displacement vectors of the rotor system, respectively, and ω is the rotational angular velocity of the rotor.

The structural parameters of the hollow axle of the SZLH420 ring die granulator are listed in Table 1. The elastic modulus, E, was 210 GPa, the material density, ρ, was 7,850 kg/m³, the Poisson's ratio, λ, was 0.3, α_{o} and β_{o} were both 0.05, and the axle rotational speed, n, was 300 r/min.

Table 1. *Structural parameters of the beam*

Element number	Outer diameter [mm]	Inner diameter [mm]	Length of element [mm]
1	120	80	45
2	120	80	45
3	150	80	45
4	150	80	45
5	150	80	45
6	150	80	45
7	190	80	60
8	200	80	50
9	200	80	50
10	230	80	110
11	560	210	10
12	600	240	10
13	640	300	10
14	680	420	20
15	666	420	8
16	652	420	8
17	640	420	8
18	580	420	85
19	580	420	85
20	600	420	30

2 MECHANICAL MODEL FOR THE COUPLED SYSTEM

2.1 Mechanical Model for the Deep Groove Ball Bearing Support

Bearings are a critical part of a rotor system, and they support and constrain the axles. The bearing parameters of the models of the two groups of deep groove ball bearings in the ring die granulator, Models 6412 and 6420, are listed in Table 2. The deep groove ball bearings consisted of an inner and an outer ring, balls, and a cage. It was assumed that the contacts between the balls and the inner and outer rings were point contacts, and the effect of centrifugal force during rotation was ignored when calculating the bearing support force. A schematic diagram of one of the deep groove ball bearings is shown in Fig. 4, in which ω_{in} represents the angular velocity of the balls on the inner ring and ω_{cage} is the rotational angular velocity of the cage. The outer ring and frame had an interference fit with a connection speed of zero. Assuming that the balls were evenly distributed in the inner and outer races, the nonlinear restoring forces in

the *x*- and *y*-directions of the deep groove ball bearing could be expressed by Eq. (4):

$$F_{\mathrm{b}}=\begin{cases}F_{\mathrm{b}x}=\sum_{j=1}^{N_{\mathrm{b}}}F_{jx}=\sum_{j=1}^{N_{\mathrm{b}}}F_j\cos\theta_j\\ F_{\mathrm{b}y}=\sum_{j=1}^{N_{\mathrm{b}}}F_{jy}=\sum_{j=1}^{N_{\mathrm{b}}}F_j\sin\theta_j\end{cases}. \quad (4)$$

In Eq. (4), $F_{\mathrm{b}x}$ and $F_{\mathrm{b}y}$ represent the supporting forces in the *x*- and *y*-directions of the bearing, respectively, N_{b} is the number of balls in the deep groove ball bearing, and θ_j is the rotation angle of the j^{th} ball at time *t* and can be expressed by Eqs. (5) and (6):

$$\theta_j=\omega_{\mathrm{cage}}\times t+\frac{2\pi}{N_{\mathrm{b}}}(j-1)\quad j=1,2,\cdots,N_{\mathrm{b}}, \quad (5)$$

$$\omega_{\mathrm{cage}}=\frac{\omega_{\mathrm{in}}\times r}{R_{\mathrm{b}}+r}. \quad (6)$$

In Eqs. (5) and (6) R_{b} is the inner radius of the outer ring of the bearing and *r* is the outer radius of the inner ring of the bearing. The contact deformations between the balls and the inner and outer rings in the deep groove ball bearing satisfy the Hertz contact theory. Therefore, the contact extrusion force, F_j, generated by the j^{th} ball on the race could be expressed by Eq. (7):

$$F_j=C_{\mathrm{b}}\times\delta_j^{3/2}\times H(\delta_j), \quad (7)$$

where C_{b} represents the Hertzian contact stiffness related to the material properties and δ_j represents the normal contact deformation between the j^{th} ball and the races. The interaction between the ball and the races can only generate a normal positive pressure. Therefore, a force exists when the normal contact deformation, δ_j, between the ball and the races is greater than zero. To determine the contact between the ball and the races, the Heaviside function was introduced:

$$H(\delta_j)=\begin{cases}1 & \delta_j>0\\ 0 & \delta_j<0\end{cases}. \quad (8)$$

For the bearing clearance, γ_0, and the *x* and *y* radial displacements, the normal contact deformation, δ_j, between the ball and the races could be expressed by Eq. (9):

$$\delta_j=x\cos\theta_j+y\sin\theta_j-\gamma_0. \quad (9)$$

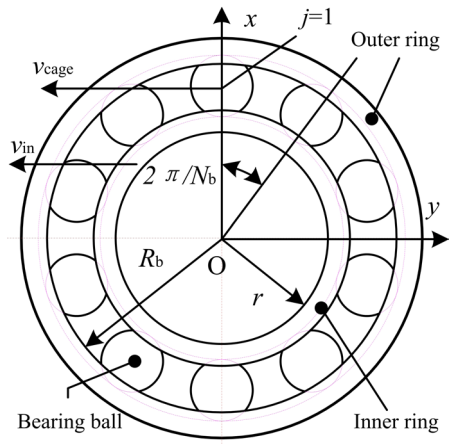

Fig. 4. *Bearing mechanical model*

Table 2. *Structural parameters of the support bearing*

Bearing *i*	1	2
Outer radius R_{b} [mm]	55.55	79
Inner radius *r* [mm]	40.65	62.4
Ball number N_{b}	19	25
Contact stiffness C_{b} [GN/m$^{3/2}$]	8.05	
Bearing clearance γ_0 [μm]	10	
Support stiffness k_i [N/m]	7×108	9×108
Brace damping C_i [Ns/m]	500	1000

2.2 Mechanical Model for the Helical Gear Mesh

The gear was treated as a thin hard disk using the lumped mass method. The mechanical model for the gear shown in Fig. 5 was developed by analysing the forces acting on the gear and decomposing them orthogonally. The mass eccentricity caused by the casting error and nonuniform gear material is represented by *e.* The geometric centre of the gear is at O_1 and the centre of mass is at O_g. The gravity of the gear itself is represented by *P.* The centrifugal force of the eccentricity of the gear rotating mass is expressed by F_e=M$e\omega^2$. At the beginning of operations, the line O_1O_g was parallel to the *x*-axis. For any *t,* the angle between O_1O_g and the *x*-axis was ωt. Since the meshing stiffness calculation based on the cumulative potential energy method and the meshing error calculation considering gear alignment and modification factors have a wide range of applications and practices **[21]** to **[23]**, the Fourier expansion calculated accordingly is as follows:

$$k(t)=k_{\mathrm{m}}+k_{\mathrm{a}}\sin(\omega t+\varphi), \quad (10)$$

where k_{m} represents the average mesh stiffness, k_{a} is the mesh stiffness variation amplitude, and

φ is the initial phase angle and is equal to 0. The comprehensive transmission error, $e(t)$, affected by the tooth profile and pressure angle errors in an external gear transmission could be expressed by Eq. (11):

$$e(t) = e_{\mathrm{r}} \sin(\omega t + \varphi), \tag{11}$$

where e_{r} is the comprehensive (general) transfer error amplitude. Then, the radial dynamic mesh force of the gear can be defined as the sum of the elastic restoring force and the damping force:

$$F_a = k(t) f(X(t), \mathrm{b}) + c_{\mathrm{m}} \dot{X}(t). \tag{12}$$

In Eq. (12), c_{m} represents the mesh damping and $f(X(t), \mathrm{b})$ is a nonlinear function. Assuming that the driving gear axle was a rigid axle and that its vibration angle displacement was negligible, the displacement function, $X(t)$, of the driven gear axle vibration and mesh error is expressed by Eq. (13):

$$X(t) = y + e(t). \tag{13}$$

The gear transmission had a certain one-sided backlash, b_0. When there were x and y vibration displacements during the gear operation, the corrected backlash, b, could be expressed by Eq. (14):

$$\begin{aligned} b &= b_0 + a_0 \cos\alpha_0 (\tan\alpha' - \tan\alpha_0 + \alpha_0 - \alpha'), \\ \alpha' &= \arccos(a_0 \cos\alpha_0 / a'), \\ a' &= \sqrt{(a_0 \cos\alpha_0 + x)^2 + (a_0 \sin\alpha_0 + y)^2}. \end{aligned} \tag{14}$$

In Eq. (14), a_0 and α_0 represent the initial centre distance and the pressure angle, respectively, and a' and α' are the centre distance and pressure angle in the actual meshing process, respectively. The nonlinear function in the dynamic mesh force equation could be expressed by Eq. (15):

$$f(X(t), b) = \begin{cases} X(t) - b & X(t) > b \\ 0 & |X(t)| \le b \\ X(t) + b & X(t) < -b \end{cases}. \tag{15}$$

The friction force of the tooth surface could be obtained from the dynamic mesh force of the gear meshing. The secondary friction force of the gear can be expressed by Eq. (16):

$$F_f = \lambda \mu F_a, \tag{16}$$

where μ is the static friction coefficient. For mesh points above a node, λ was assigned a value of 1, otherwise, it was assigned a value of 1. The gear forces, F_{gx} and F_{gy}, in the x- and y- directions were obtained from Eq. (17):

$$\begin{aligned} F_{gx} &= \mathrm{M} e \omega^2 \sin(\omega t) + F_f, \\ F_{gy} &= -\mathrm{M} e \omega^2 \cos(\omega t) + F_a - P. \end{aligned} \tag{17}$$

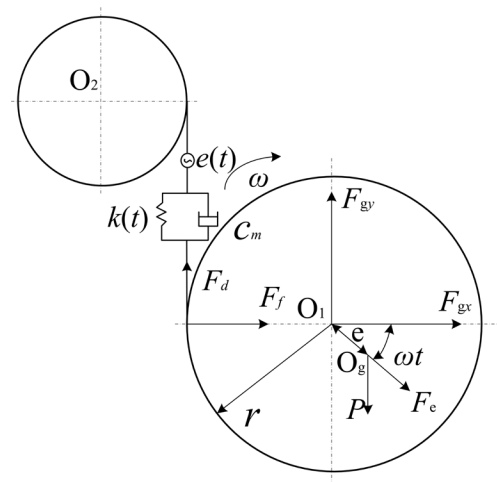

Fig. 5. *Gear mechanical mode*

The mass, M, of the ring die granulator gear was 113 kg, the initial one-sided backlash, b_0, was 10 μm, the static friction coefficient, μ, was 0.3, and the mass eccentricity, e, was 2 mm. The rest of the helical gear parameters are listed in Table 3.

Table 3. *Structure parameters of helical gear*

Gear i	1	2
Number of teeth z_i	23	120
The modulus m_{n} [mm]	4	4
Pressure angle α [°]	20	
Spiral angle β [°]	18	
Tooth width B [mm]	150	
k_{m} [N/m]	6.3×106	
k_{a} [N/m]	3.2×105	
e_{r} [mm]	2.2×10-5	
C_{m} [Nm/s]	117	

2.3 Mechanical Model for External Excitation

The extrusion force is an important cause of the vibration in a ring die granulator rotor. Developing an effective extrusion mechanical model is the key step for accurately analysing the dynamic characteristics of the ring die granulator rotor. As shown in Fig. 6, during relative motion of the ring die and the pressing roller, the material entered the gap between the die roller and the rotation of the ring die and was extruded to reach the extrusion density. The material extrusion area was

divided into a compression area and an extrusion area, which corresponded to the central angles, θ_t and θ_{max}, respectively. The extrusion force on the inner surface of the ring die increased as the extrusion density of the material increased, and it tended to be stable after reaching the extrusion density. The extrusion density of the material was largest at the location where the die-roller gap was a minimum, that is, the extrusion force was largest. Assuming that the frictional force generated by the extrusion of the material restrained the relative sliding between the pressure roller and the ring die, ignoring the rotational inertia force of the material, and treating the ring die and the pressure roller as rigid bodies, the force distribution diagram was obtained for the ring die, as shown in Figure 6. F_{hx} and F_{hy} represent the components of the extrusion force in the x- and y-directions, respectively, f_x and f_y are the components of the friction force in the x- and y-directions, respectively, e is the distance between the roller and the centre of the ring die, r_h is the inner diameter of the ring die, r_r represents the outer diameter of the roller, d is the thickness after compression and extrusion, and h is the thickness of the uncompressed material.

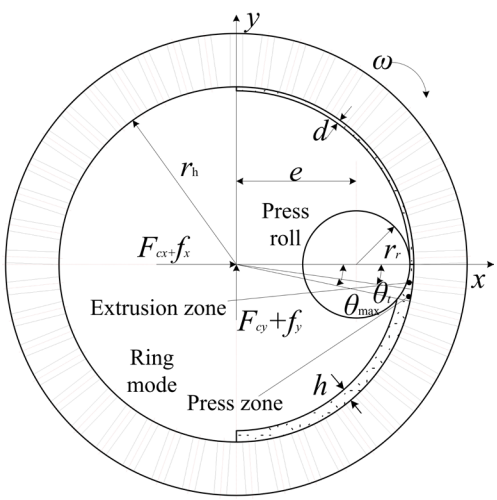

Fig. 6. *Mechanical model of ring mode*

In a ring die granulator, a gap is present between the pressing roller and the ring die to avoid rigid impacts caused by the vibration of the ring die. As the material is squeezed by the pressing roller, plastic deformation occurs in the extrusion area, and the density of the material is inversely proportional to the gap between the die and the roller. Because this gap exists, in addition to the material compressed into the die hole, an adhesion layer of the material is formed on the inner surface of the ring die after extrusion. Therefore, material extrusion occurs on the adhesion layer and the material density of the adhesion layer is equal to the theoretical discharge density. The relationship between the density of the material discharged from the ring die granulator and the ratio of the density of the initial material, $\gamma(\theta)$, and the central angle, θ, of the ring die can be expressed by Eq. (18):

$$\gamma(\theta)=\frac{\mathrm{h}}{\mathrm{r_h}+\mathrm{e}\cos\theta-\sqrt{\mathrm{r_r^2}-\mathrm{e^2}\sin^2\theta}-\mathrm{d}}. \quad (18)$$

During material extrusion, the extrusion force varies exponentially with the material density and can therefore be estimated according to the material properties. An exponential function can be used to describe the relationship between the extrusion force, P, and the material density with the central angle, θ, of the ring die:

$$P(\theta)=\lambda e^{k[\gamma(\theta)-1]}. \quad (19)$$

In Eq. (19), λ and k are constants. In an actual granulation process, the theoretical discharge density of the adhesion layer is less than the actual discharge density and the surface extrusion force of the ring die is greater than the extrusion force of the adhesion layer. Therefore, Eq. (20) was used in this study to correct the surface extrusion force of the ring die:

$$P'(\theta)=P(\theta)\frac{\mathrm{r_h}}{\mathrm{r_h}-\mathrm{d}}. \quad (20)$$

The external excitation force of the ring die was obtained from a definite integral of the extrusion force on the inner surface of the ring die at the extrusion angles θ_t and θ_{max}. Then, the orthogonal components, F_{cx} and F_{cy}, of the centre stress of the ring die could be expressed by Eq. (21):

$$\left.\begin{aligned}F_{cx}&=P_t\mathrm{br_h}\theta_t\cos\frac{\theta_t}{2}+\int_{\theta_t}^{\theta_{max}}\mathrm{b}(\mathrm{r_h}-\mathrm{d})P'(\theta)\cos\theta d\theta\\F_{cy}&=P_t\mathrm{br_h}\theta_t\sin\frac{\theta_t}{2}+\int_{\theta_t}^{\theta_{max}}\mathrm{b}(\mathrm{r_h}-\mathrm{d})P'(\theta)\sin\theta d\theta\end{aligned}\right\}. \quad (21)$$

According to the acting angle of the ring die extrusion zone and the cosine theorem, the central angle of the extrusion circle could be expressed by Eq. (22):

$$\theta_t = \arccos\left\{\frac{\left[r_h-\left(d+h/\gamma_t\right)\right]^2+e^2-r_r^2}{2\left[r_h-\left(d+h/\gamma_t\right)\right]e}\right\},$$
$$\gamma_t = \frac{\ln P'(\theta)-\ln\lambda}{k}+1. \quad (22)$$

When γ_t=1, the maximum extrusion central angle, θ_{max}, could be obtained. The static friction coefficient, μ, was used to describe the static friction between the material and the ring die, so the resultant external force acting on the position of the ring die could be expressed by Eq. (23):

$$\left.\begin{aligned} F_{hx} &= F_{cx}+\mu F_{cy} \\ F_{hy} &= F_{cy}+\mu F_{cx} \end{aligned}\right\}. \quad (23)$$

When the ring die had x and y vibration displacements, the dynamic eccentricity value of the die roller was as shown in Eq. (24). By substituting the dynamic eccentricity, e', into the theoretical derivation described above, the dynamic random extrusion force that varied with the vibration displacement was obtained.

$$e' = \sqrt{e^2+y^2}+x. \quad (24)$$

The eccentric distance, e, of the die roller of the ring die granulator was 0.1 m. The inner diameter, r_h, of the ring die was 0.21 m. The outer diameter, r_r, of the pressing roller was 0.103 m. The thickness, d, after molding and extrusion was 0.004 m. The thickness, h, of the uncompressed material was 0.02 m. The width, b, of the ring die was 0.12 m. The extrusion calculation parameters λ and k were 1,0000 and 3, respectively, and the static friction coefficient, μ, was 0.3.

3 EXPERIMENTAL VERIFICATION

To verify the accuracy and precision of the dynamic model, a SZLH420 ring die granulator was tested in actual production. Vibration at the ring die position was not easy to test because of overhang, rotation, and limited space. The test was conducted at the bearing position 1 (node 2). The test results were compared with theoretical calculation results. In the test, an A302 wireless acceleration measurement sensor from Beijing Bitron Co., Ltd. was used for signal acquisition, a BS951-T wireless gateway was used for data transmission, and a portable computer was used for data processing and analysis. The specific experimental scheme and the schematic diagram of the test setup are shown in Fig. 7.

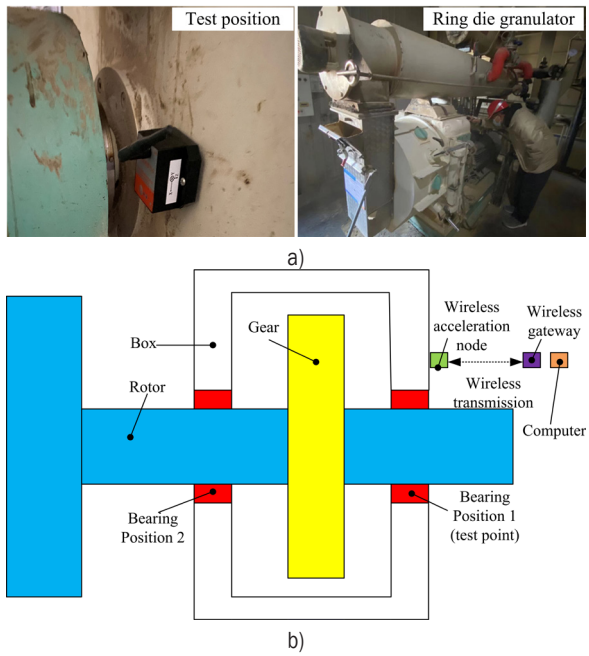

Fig. 7. *Testing program; a) testing program, and b) schematic diagram of test setup*

The acceleration data in the x- and y-directions were collected during the experiment. The vibration displacement, velocity, and acceleration curves in the time domain were obtained by processing the data with data analysis software, and the vibration curves in the frequency domain were obtained from fast Fourier transforms. The results are shown in Fig. 8a. The Newmark–β method was used to solve the nonlinear dynamics equation of the coupled system. The curves in the frequency and time domains for node 2 at the bearing position are shown in Fig. 8b. Using the stable data and comparing the experimental results and theoretical calculations, it was evident that the frequency errors and amplitudes at the peaks in the frequency-domain graphs between the experimental and theoretical results did not exceed 5 %, and the vibration amplitudes for the curves in the time domain did not exceed 10 %. The experimental results were affected by various excitation disturbances, such as those from the motor, feeder, and modulator. As a result, the experimentally measured time-domain and frequency-domain curves were more complex and the amplitudes were overestimated. The results show that the nonlinear dynamics model for the coupled overhung rotor established during this study is highly accurate and can be used for predicting system dynamic characteristics.

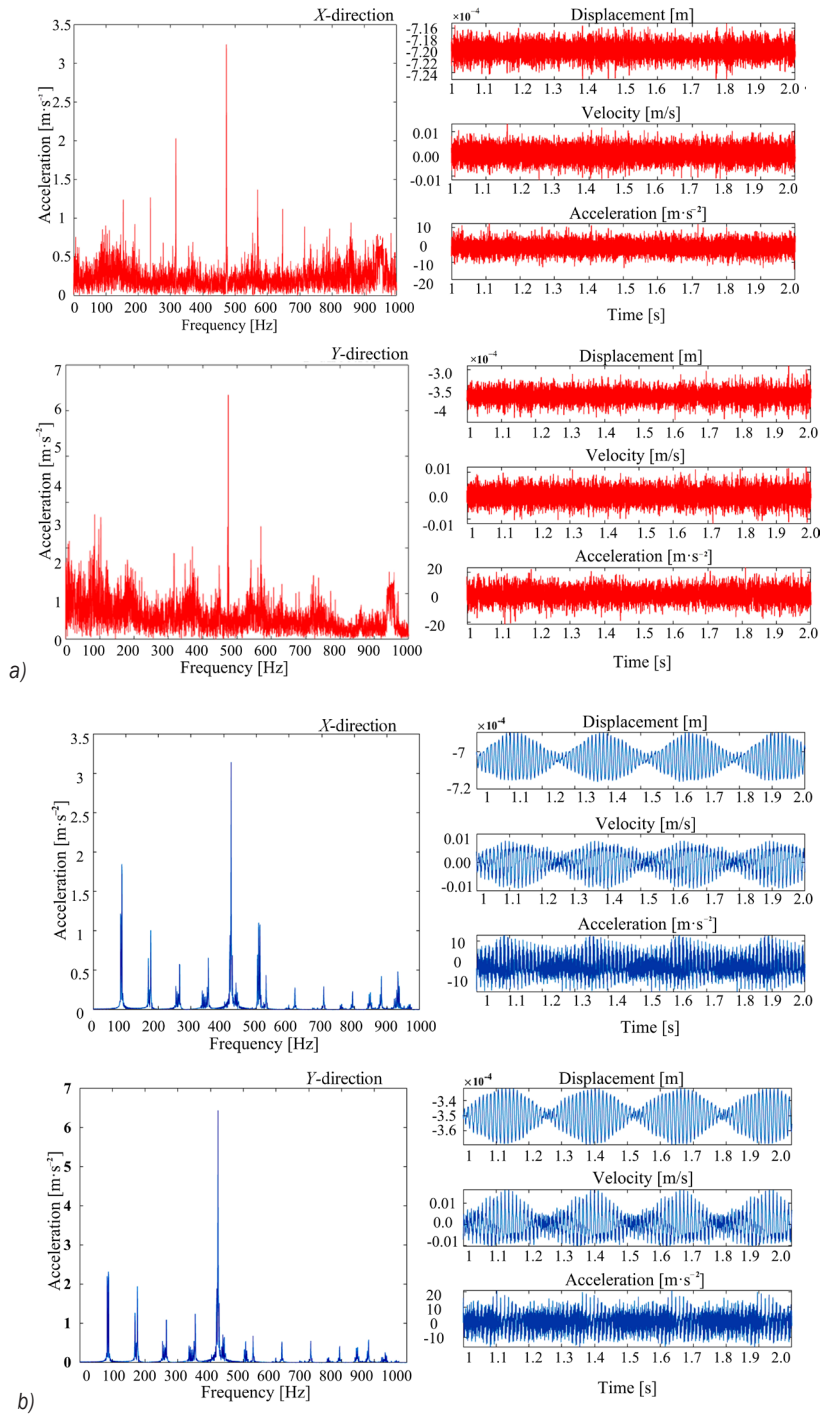

Fig. 8. *Comparison between vibration response test and theoretical results of ring die pelletizer system; a) test results, and b) theoretical results*

4 ANALYSES AND PREDICTIONS OF DYNAMIC CHARACTERISTICS OF THE COUPLED ROTOR MODEL

Ring dies in the rotor systems of ring die granulators are prone to wear. According to actual production field research, the replacement cost of a ring die accounts for more than 30 % of the production cost of the entire factory. Nonlinear vibrations at a ring die cause extreme extrusion or severe wear of the ring die, which can lead to damage of the ring die. Several

rotor parameters for the horizontal ring die granulator were selected for this study: a rotational speed of n = 300 r/min, a ring die roller eccentricity of e = 0.1 m, a bearing clearance of γ_0 = 10 μm, and a length of axle segment 7 of l_7 = 60 mm. Time-domain curves, frequency-domain curves, phase diagrams, and Poincaré section diagrams for the dynamic response in both directions at the ring mode position (node 19) are shown in Fig. 9. The figure shows that the maximum vibration displacement response in the x-direction was approximately 2.09 mm and the maximum vibration displacement response in the y-direction was 2.12 mm. These results occurred because the rotor system was subjected to the combined effects of gravity in the y-direction, the ring die force, the mesh force, and the bearing force. The time-domain curves were transformed into frequency-domain curves by fast Fourier transformation (FFT). The main vibration frequencies and amplitudes in both directions were the same, and the frequency division phenomenon caused by various external forces occurred near the low frequency. The phase diagrams were approximately closed circles and showed weak disorder and trends from quasi-periodic motion to chaotic motion. The Poincaré section was an approximate point system in a quasi-periodic motion. The current rotor system ran relatively smoothly.

4.1 Effect of the distance between the bearings on the system dynamics

For considerations of space and cost in the structural design of a granulator, the supporting distance between the two bearings of the overhung rotor should not be too large. The effect of changing the supporting distance between the two bearings,

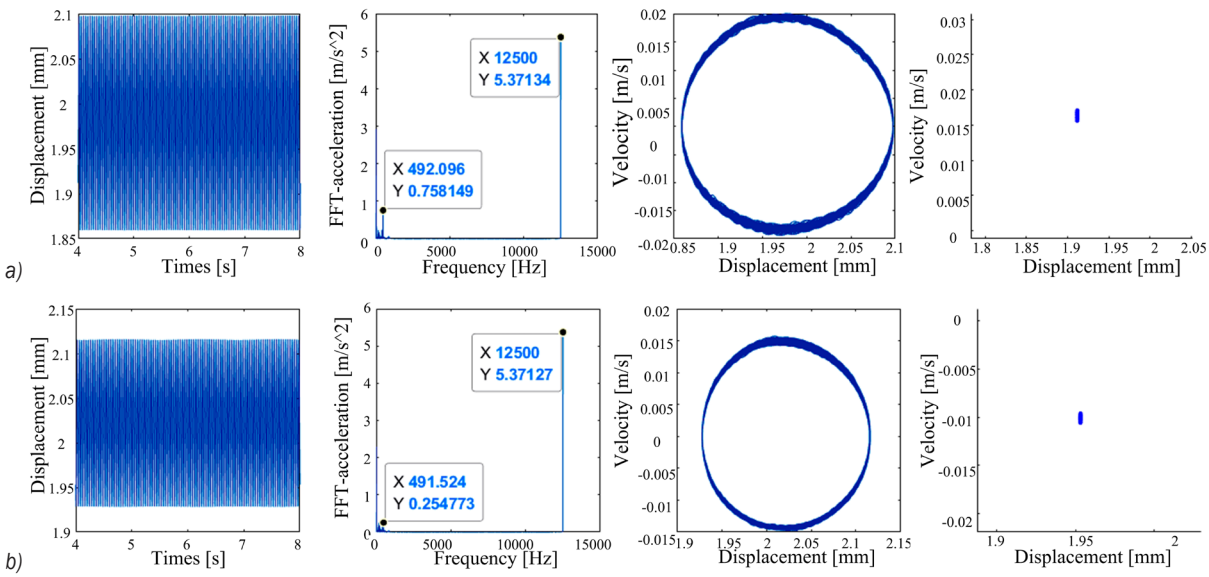

Fig. 9. *Displacement response diagram, FFT diagram, phase diagram and Poincaré section diagram at the actual ring mode position; a) x-direction, and b) y-direction*

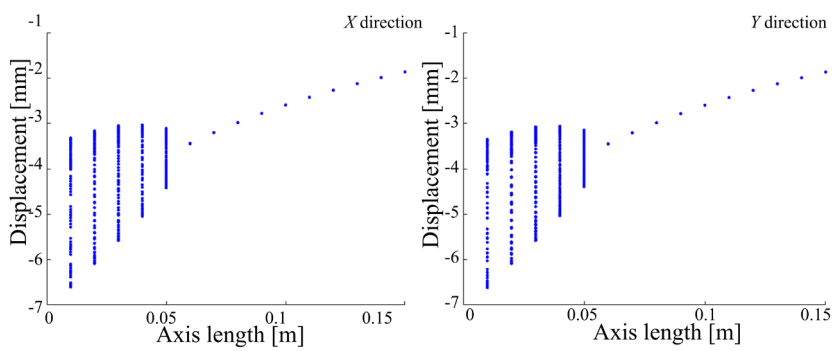

Fig. 10. *Bearing support distance variation of the rotor system is illustrated*

namely, the length of axle segment 7, on the dynamic response of the overhung rotor system is shown as a bifurcation diagram in Fig. 10. The diagram shows that as the distance between the two bearings increased, the system motion gradually changed from complex chaotic motion to quasi-periodic motion, and to period-1 motion at l_7 = 90 mm. Therefore, an appropriate increase in the bearing support distance is beneficial for optimizing the dynamic response of the system at the ring die location. Figs. 11a and b show that when l_7 = 120 mm, the maximum vibration displacement responses in the *x*- and *y*-directions were approximately 1.88 mm and 1.92 mm, respectively. The time-domain responses were significantly better than those in the actual granulator. The FFT curves show that the vibration amplitudes in both directions were significantly reduced, and the frequency division was weakened. The phase diagrams were

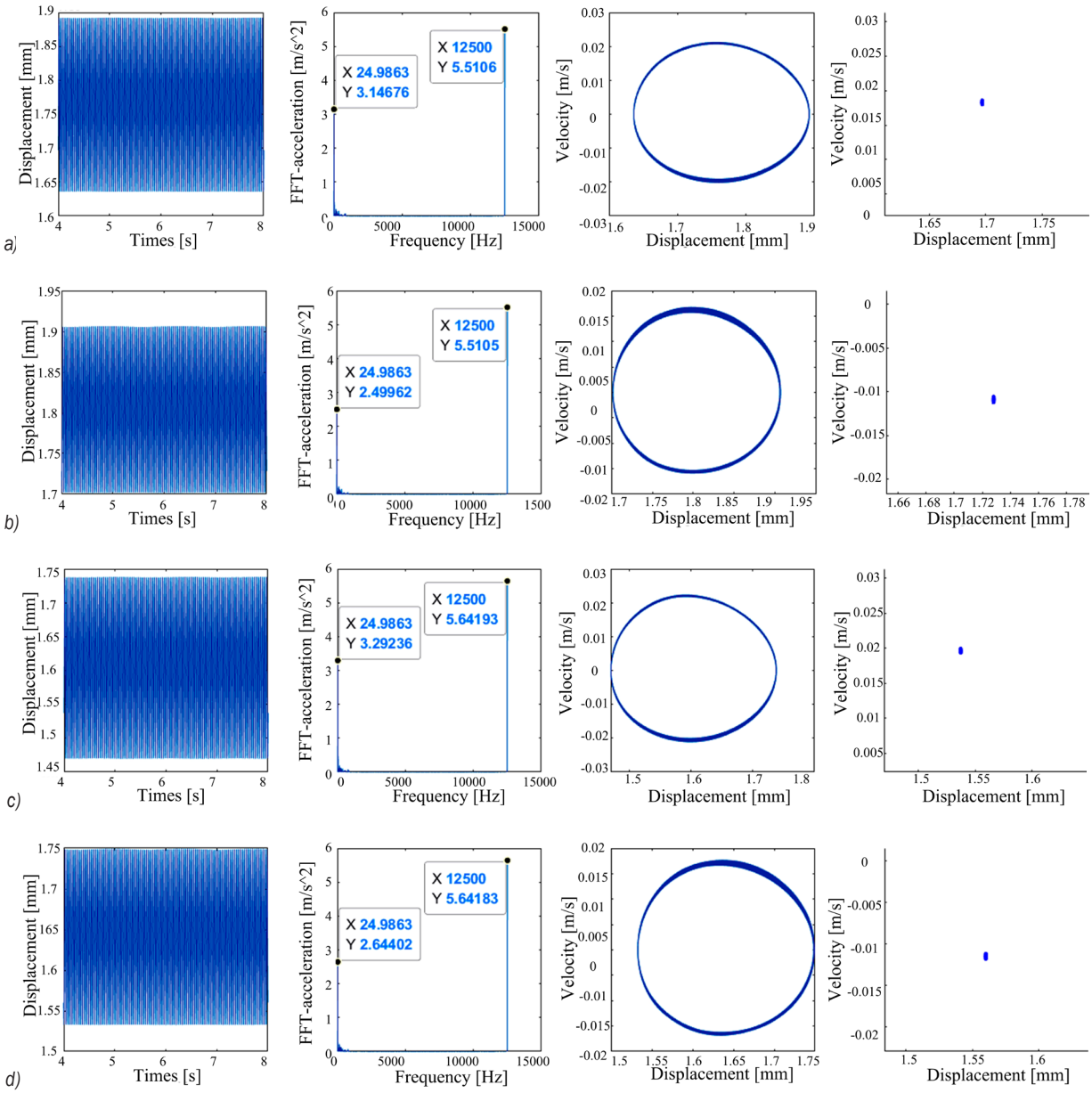

Fig. 11. *Displacement response diagram, FFT diagram, phase diagram and Poincaré section diagram at the position of predicted ring mode; a) axis segment element 7 is 90 mm in X-direction, b) axis segment element 7 is 90 mm in Y-direction, c) axis segment element 7 is 120 mm in X-direction, and d) axis segment element 7 is 90 mm in Y-direction*

approximately closed circles, the turbulence was reduced, and the periodic motion of the system tended to be stable. The Poincaré sections were point systems with quasi-periodic motion, and the current rotor system ran more smoothly. Figs. 11c and d show that the response of the rotor system was further optimized when l_7 = 80 mm. This phenomenon occurred because an appropriate increase in the bearing support distance was beneficial for optimizing the effect of the bending-torsional coupling of the system.

4.2 Effect of Roller Eccentricity on the System Dynamics

To avoid rigid collisions during the ring die assembly process, a gap is present between the die and the roller. The wear of the ring die during production operations leads to increases in the gap between the die and the roller, which causes decreases in the eccentricity of the press roller. When only the eccentricity of the rollers was varied, the effect of the roller eccentricity on the dynamic response of the overhung rotor system was predicted, and the resulting bifurcation diagrams are shown in Fig. 12. The figure shows that as the roller eccentricity increased, the system motion gradually changed from period-1 motion to quasi-periodic motion to chaotic motion. The eccentric distance affects the granulation efficiency. Appropriately reducing the eccentric distance of the roller is beneficial for optimizing the response of the rotor system. Figs. 13a and b show that when e = 0.099 m, the maximum vibration displacement responses were approximately 1.91 mm and 1.92 mm in the x- and y-directions, respectively. The time-domain responses were considerably better than those of the actual granulator. The FFT curves show that the vibration amplitudes in both directions were reduced, and the frequency division was weakened. The phase diagrams were approximately closed circles, the disorder phenomenon was reduced, and the periodic motion of the system tended to be stable. The Poincaré sections were point systems with quasi-periodic motion, and the current rotor system ran more smoothly. Figs. 13c and d shows that at e = 0.101 m, the response of the rotating system deteriorated, and the maximum vibration displacement responses were approximately 2.18 mm and 2.21 mm in the x- and y-directions, respectively. The time-domain responses were higher than the actual granulator amplitudes. The FFT curves show that the vibration amplitudes in both directions increased, the frequency division was more severe, the phase diagrams appeared severely disordered, and the system motion changed from quasi-periodic motion to mixed motion. The Poincaré sections were approximately closed cycles connected by points, representing quasi-periodic motion, and the current rotor system was unstable. This phenomenon was caused by the effect of eccentricity on the external extrusion load on the surface of the ring die and provides an important theoretical basis for adjusting the gap between the roller and the die during production operations.

4.3 Effect of Bearing Clearance on the System Dynamic Response

A strong nonlinearity exists in the bearing clearance during the bearing assembly process. The bearing clearance increases due to wear during operation. When only the bearing clearance was changed, the effect of the bearing clearance on the dynamic response of the overhung rotor system was predicated, and the resulting bifurcation diagrams are shown in Fig. 14. The figure shows that as the bearing clearance increased, the system motion changed from period-1 motion to quasi-periodic motion to chaotic motion. Regular bearing lubrication and replacement can ensure a small bearing clearance, which is conducive for optimizing the response of the rotor system. Figs. 15a and b show that when γ_0 = 40 μm, the maximum vibration displacement responses were approximately 2.19 mm and 2.22 mm in the x- and y-directions, respectively, and the time-domain response amplitudes were greater than those of the actual granulator. The FFT curves show that the vibration amplitudes in both directions increased, the low-frequency vibrations were noticeable, and the frequency division was strengthened. The phase diagrams were approximately closed ellipses, the turbulent phenomenon increased, and the periodic motion of the system tended to be chaotic. The Poincaré sections were approximately asymptotes, the system motion changed from quasi-periodic to chaotic motion, and the current rotor system operation gradually became unstable. Figs. 15c and d show that when γ_0 = 80 μm, the response of the rotating system deteriorated further, with maximum vibration displacement responses of approximately 2.32 mm and 2.34 mm in the x- and y-directions, respectively. This phenomenon was caused by the bearing clearance affecting the bearing support force of the rotor system, and it provides an important theoretical basis for equipment operation and maintenance as well as regular part and component replacement.

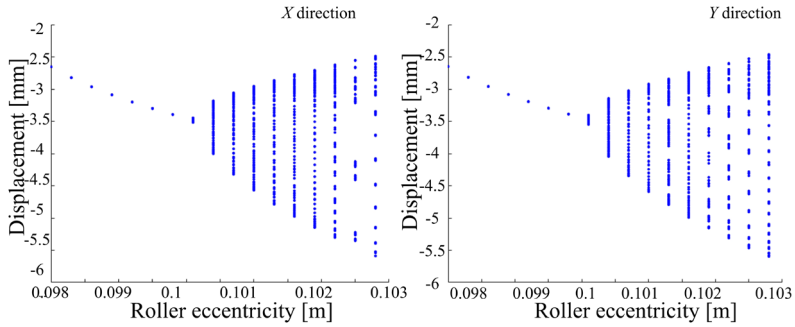

Fig. 12. *Die roll eccentricity distance variation of the rotor system is illustrated*

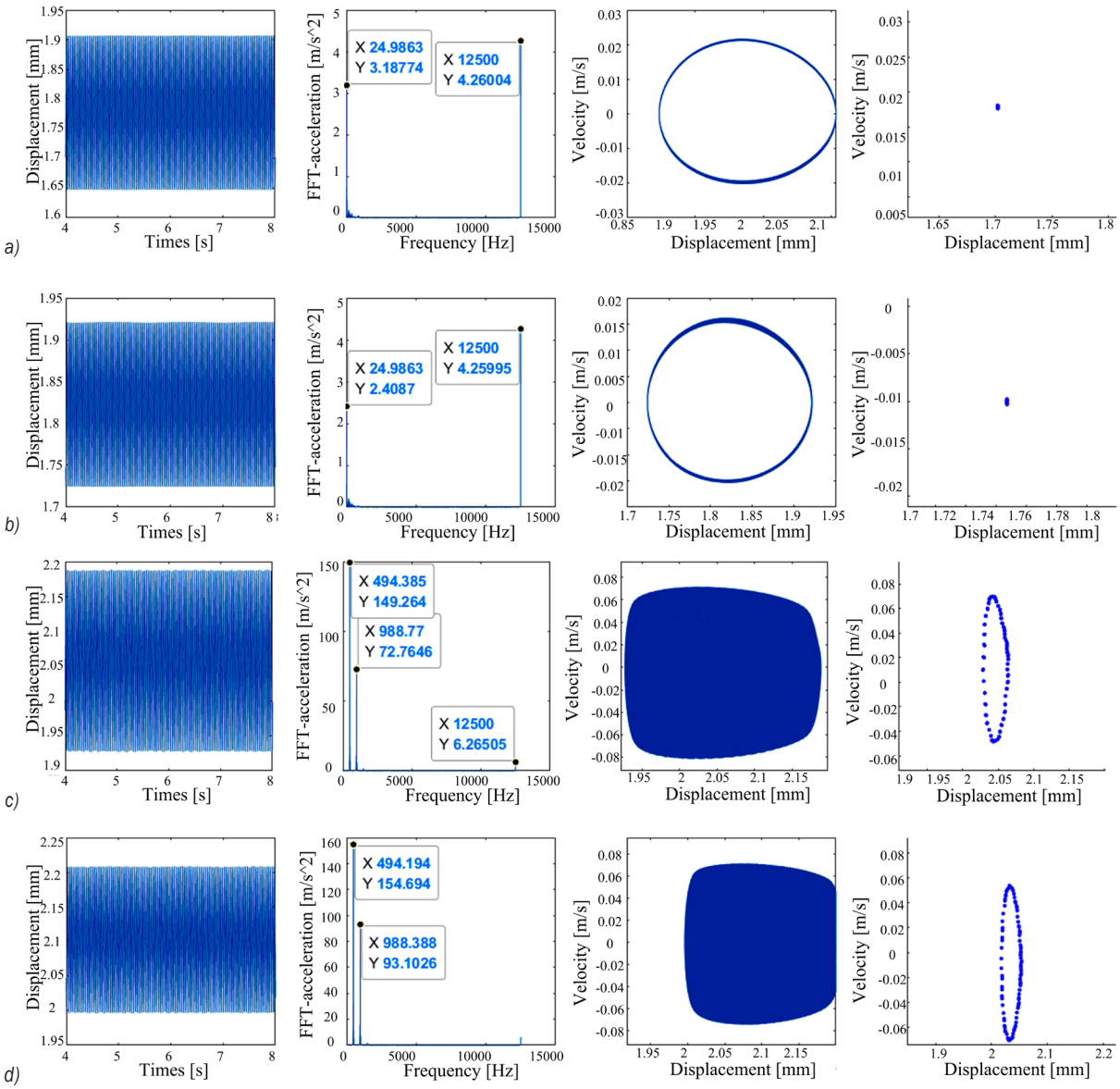

Fig. 13. *Displacement response diagram, FFT diagram, phase diagram and Poincaré section diagram at the position of predicted ring mode; a) ring roller eccentricity is 0.099 m in X-direction, b) ring roller eccentricity is 0.099 m in Y-direction, c) ring roller eccentricity is 0.101 m in X-direction, and d) ring roller eccentricity is 0.101m in Y-direction*

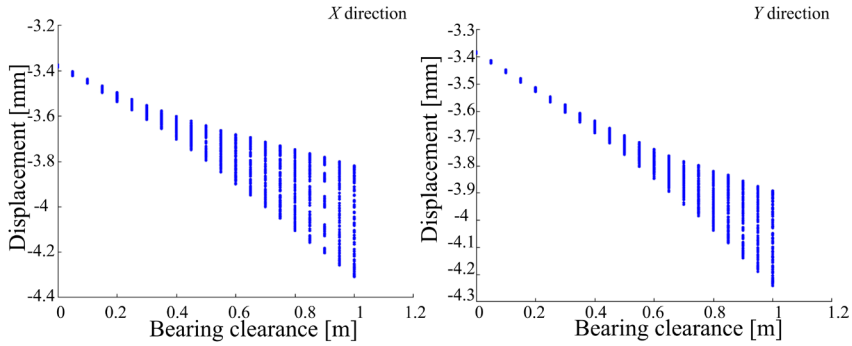

Fig. 14. *Bearing clearance variation of the rotor system*

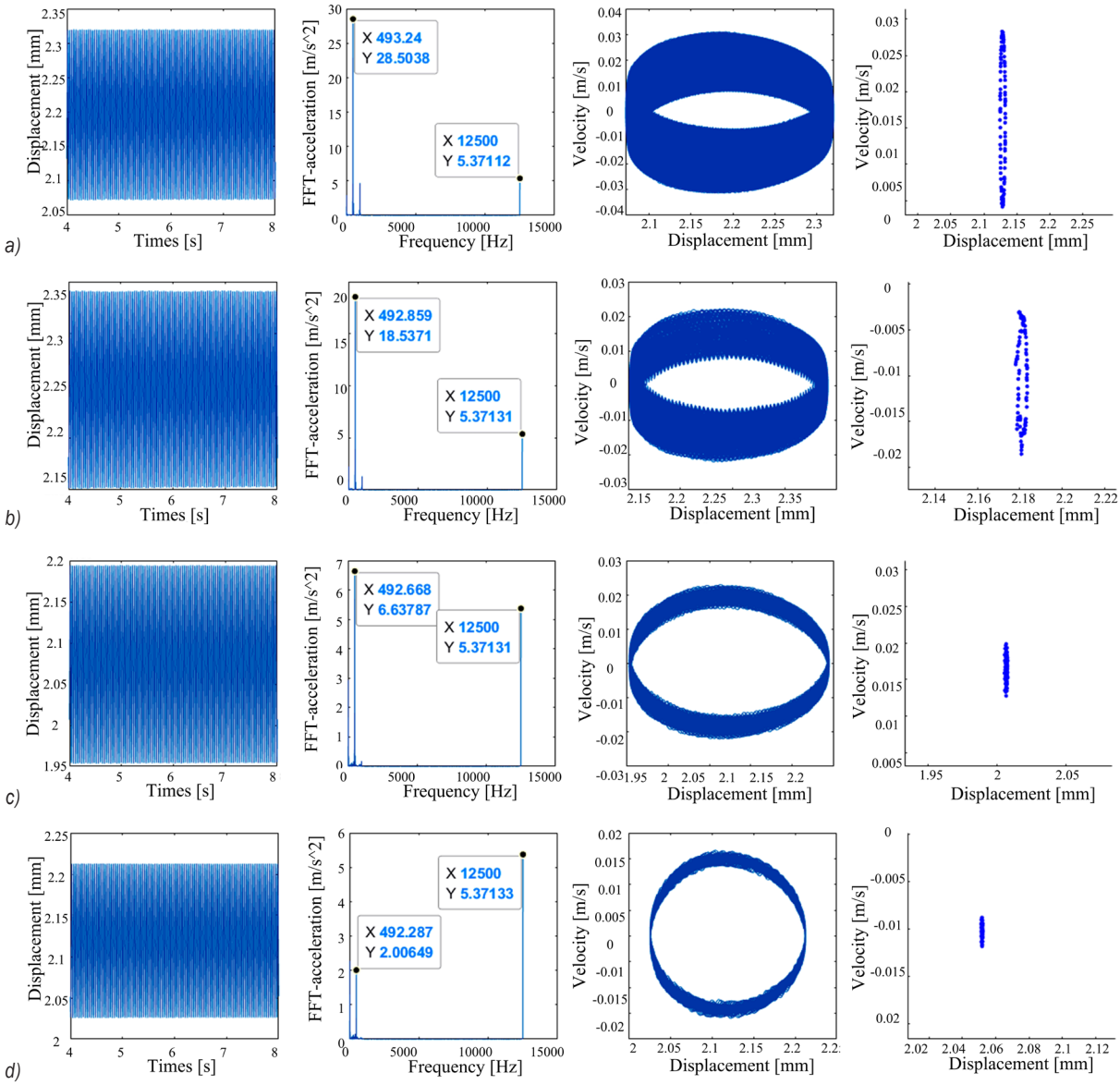

Fig. 15. *Displacement response diagram, FFT diagram, phase diagram and Poincaré section diagram at the position of predicted ring mode; a) bearing clearance is 40 μm in X-direction, b) bearing clearance is 40 μm in Y-direction, c) bearing clearance is 80 μm in X-direction, and d) bearing clearance is 80 μm in Y-direction*

5 CONCLUSIONS

In this paper, experimental verification was conducted using a real-world operating ring die granulator, and the experimental results were compared with the theoretical calculation results to verify the validity and accuracy of the theoretical model. At the same time, the correctness and practicability of the extrusion mechanics model, the gear meshing model, the bearing support model, and the multi-excitation coupling model of the rotor system are also verified. This is helpful when solving the dynamics of complex structure and excited rotor. Finally, according to the theoretical model, for the strong nonlinear factors, such as the bearing support distance, the roller eccentricity, and the bearing clearance variation, dynamic response analyses were performed using bifurcation diagrams and the effects of their parameters on rotor performance were determined. The results of this study can be summarized into three primary points:

1. The increase of bearing support distance is beneficial to the optimization of dynamic response characteristics of the system. When bearing support distance is short, the response becomes complicated and chaotic motion is easy to appear. When the bearing distance increases by 120 mm, the displacement amplitudes in *x*- and *y*- directions decrease by 0.35 mm and 0.37 mm, respectively, and the dynamic performance indexes of the system are optimized. Therefore, reasonable rotor structure design and bearing support distance selection are of great significance when optimizing system response and improving system stability.
2. The reduction of eccentricity of roll die is beneficial to the optimization of system response. Comparisons of the frequency-domain curves, the phase diagrams, and the Poincaré section diagrams showed that as the eccentric distance of the pressure roller decreased, the amplitude of the system response was reduced, the disorder phenomenon was weakened, and the dynamic performance indicators were optimized. The eccentric distance is a key factor affecting the granulation efficiency and quality. Therefore, it is important to select an appropriate eccentricity for the rollers to optimize the system response and improve the system productivity.
3. The reduction of bearing clearance is beneficial to the optimization of dynamic response characteristics of the system. Comparisons of the frequency-domain curves, the phase diagrams, and the Poincaré section diagrams showed that as the bearing clearance decreased, the amplitudes of the system response decreased, the disorder phenomenon was weakened, and the dynamic performance indicators were optimized. The bearing clearance is a key factor affecting the stability of the rotor system. Therefore, regular bearing maintenance and replacement is important for optimizing the response of the rotor system and improving the reliability of the system.

6 ACKNOWLEDGEMENTS

The authors acknowledge the financial support from the National Natural Science Foundation of China (Grant No. 52065050) & Basic research funds for universities directly under the Inner Mongolia Autonomous Region of China (Grant No. JY20220377).

8 REFERENCES

[1] Schwarz, S., Grillenberger, H., Tremmel, S., Wartzack, So. (2022). Prediction of rolling bearing cage dynamics using dynamic simulations and machine learning algorithms. *Tribology Transactions*, vol. 62, no. 2, p. 225-241, **DOI:10.1080/10402004.2021.1934618**.

[2] Cai, Z., Lin, C. (2017). Dynamic model and analysis of nonlinear vibration characteristic of a curve-face gear drive. *Strojniški vestnik - Journal of Mechanical Engineering*, vol. 63, no. 3, p. 161-170, **DOI:10.5545/sv-jme.2016.3859**.

[3] Cui, Y., Deng, S., Niu, R., Chen, G. (2018). Vibration effect analysis of roller dynamic unbalance on the cage of high-speed cylindrical roller bearing. *Journal of Sound and Vibration*, no. 434, p. 314-335, **DOI:10.1016/j.jsv.2018.08.006**.

[4] Smagala, A., Kecik, K. (2021). Nonlinear dynamics analysis of a rolling bearing. *Journal Européen des Systèmes Automatisés*, vol. 54, no. 1, p. 21-26, **DOI:10.18280/JESA.540103**.

[5] Kurvinen, E., Viitala, R., Choudhury, T., Heikkinen, J., Sopanen, J. (2020). Simulation of subcritical vibrations of a large flexible rotor with varying spherical roller bearing clearance and roundness profiles. *Machines*, vol. 8, no. 2, art. ID 28, **DOI:10.3390/machines8020028**.

[6] Luo, W, Yan, C., Yang, J., Liu, Y., Wu, L. (2021). Vibration response of defect-ball-defect of rolling bearing with compound defects on both inner and outer races. *IOP Conference Series: Materials Science and Engineering*, vol. 1207, no. 1, **DOI:10.1088/1757-899X/1207/1/012006**.

[7] Bavi, R., Hajnayeb, A., Sedighi, H.M., Shishesaz, M. (2022). Simultaneous resonance and stability analysis of unbalanced asymmetric thin-walled composite shafts. *International Journal of Mechanical Sciences*, vol. 217, art. ID 107047, **DOI:10.1016/J.IJMECSCI.2021.107047**.

[8] Wang, P., Xu, H., Yang, Y., Ma, H., He, D., Zhao, X. (2022). Dynamic characteristics of ball bearing-coupling-rotor system

with angular misalignment fault. *Nonlinear Dynamics*, vol. 108, p. 3391-3415, **DOI:10.1007/S11071-022-07451-1**.

[9] Liu, J., Ding, S., Wang, L., Li, H., Xu, J. (2020). Effect of the bearing clearance on vibrations of a double-row planetary gear system. *Proceedings of the Institution of Mechanical Engineers, Part K: Journal of Multi-body Dynamics*, vol. 234, no. 2, **DOI:10.1177/1464419319893488**.

[10] Chen, Z., , J., Wang, K., Zhai, W. (2021). An improved dynamic model of spur gear transmission considering coupling effect between gear neighboring teeth. *Nonlinear Dynamics*, vol. 106, p. 339-357, **DOI:10.1007/S11071-021-06852-Y**.

[11] Zheng X., Luo, W., Hu, Y., He, Z., Wang, Sg. (2022). Study on the mesh stiffness and nonlinear dynamics accounting for centrifugal effect of high-speed spur gears. *Mechanism and Machine Theory*, vol. 170, art. ID 104686, **DOI:10.1016/j.mechmachtheory.2021.104686**.

[12] Zhu, L.-Y., Shi, J.-F., Gou, X.-F. (2020). Modeling and dynamics analyzing of a torsional-bending-pendular face-gear drive system considering multi-state engagements. *Mechanism and Machine Theory*, vol. 149, art. ID 103790, **DOI:10.1016/j.mechmachtheory.2020.10.103790**.

[13] Shi, Z., Li, S. (2022). Nonlinear dynamics of hypoid gear with coupled dynamic mesh stiffness. *Mechanism and Machine Theory,* vol. 168, art. ID 104589, **DOI:10.1016/j.mechmachtheory.2021.104589**.

[14] Hajnayeb, A., Sun, Q. (2022). Study of gear pair vibration caused by random manufacturing errors. *Archive of Applied Mechanics*, vol. 92, p. 1451-1463, **DOI:10.1007/S00419-022-02122-4**.

[15] Liu, P., Zhu, L., Gou, X., Shi, J., Jin, G. (2021). Dynamics modeling and analyzing of spur gear pair with pitch deviation considering time-varying contact ratio under multi-state meshing. *Journal of Sound and Vibration*, vol. 513, art. ID 116411, **DOI:10.1016/j.jsv.2021.116411**.

[16] Xu, H.g, Yang, Y., Ma, H., Luo, Z., Li, X., Han, Q., Wen, B. (2022). Vibration characteristics of bearing-rotor systems with inner ring dynamic misalignment. *International Journal of Mechanical Sciences*, vol. 230, art. ID 107536, **DOI:10.1016/j.ijmecsci.2022.107536**.

[17] Cirelli, M., Valentini, P.P., Pennestrì, E. (2019). A study of the non-linear dynamic response of spur gear using a multibody contact based model with flexible teeth. *Journal of Sound and Vibration*, vol. 445, p. 148-167, **DOI:10.1016/j.jsv.2019.01.019**.

[18] Cirelli, M., Giannini, O., Valentini, P.P., Pennestrì, E. (2020). Influence of tip relief in spur gears dynamic using multibody models with movable teeth. *Mechanism and Machine Theory*, vol. 152, art. ID 103948, **DOI:10.1016/j.mechmachtheory.2020.103948**.

[19] Mo, S., Zhang, T., Jin, G.-G., Cao, X.-L., Gao, H.-J. (2020). Analytical investigation on load sharing characteristics of herringbone planetary gear train with flexible support and floating sun gear. *Mechanism and Machine Theory*, vol. 144, art. ID 103670, **DOI:10.1016/j.mechmachtheory.2019.103670**.

[20] Mo, S., Yue, Z., Feng, Z., Shi, L., Zou, Z., Dang, H. (2020). Analytical investigation on load-sharing characteristics for multi-power face gear split flow system. *Journal of Mechanical Engineering Science*, vol. 234, no. 2, **DOI:10.1177/0954406219876954**.

[21] Dai, H., Long, X., Chen, F., Xun, C. (2021). An improved analytical model for gear mesh stiffness calculation. *Mechanism and Machine Theory*, vol. 159, art. ID 104262, **DOI:10.1016/j.mechmachtheory.2021.104262**.

[22] Sun, Y., Ma, H., Huangfu, Y., Chen, K., Che, L.Y., Wen, B. (2018). A revised time-varying mesh stiffness model of spur gear pairs with tooth modifications. *Mechanism and Machine Theory*, vol. 129, p. 261-278, **DOI:10.1016/j.mechmachtheory.2018.08.003**.

[23] Chang-Jian, C.W. (2010). Strong nonlinearity analysis for gearbearing system under nonlinear suspension-bifurcation and chaos. *Nonlinear Analysis: Real World Applications*, vol. 11, no. 3, p. 1760-1774, **DOI:10.1016/j.nonrwa.2009.03.027**.

[24] Liu, J., Na, R., Cen, H. (2020). Modelling and simulation of extrusion force in biomass pelletisation by ring die pellet mill. *International Journal of Simulation and Process Modelling*, vol. 15, no.5, p. 484-490, **DOI:10.1504/ijspm.2020.110927**.

[25] Peter, S., Lammens, R.F., Steffens, K.-J. (2010). Roller compaction/Dry granulation: Use of the thin layer model for predicting densities and forces during roller compaction. *Powder Technology*, vol. 199, no. 2, p. 165-175, **DOI:10.1016/j.powtec.2010.01.002**.

[26] Lei, T., Zheng, Y., Yu, R., Yan, Y., Xu, B. (2022). Dynamic response of slope inertia-based Timoshenko beam under a moving load. *Applied Sciences*, vol. 12, no. 6, art ID 3045, **DOI:10.3390/APP12063045**.

[27] Gómez-Silva, F., Zaera, R. (2022). Dynamic analysis and non-standard continualization of a Timoshenko beam lattice. *International Journal of Mechanical Sciences*, vol. 214, art. ID 106873, **DOI:10.1016/J.IJMECSCI.2021.106873**.

[28] Zhan, D., Jiang, S., Niu, J., Sun, Y. (2020). Dynamics modeling and stability analysis of five-axis ball-end milling system with variable pitch tools. *International Journal of Mechanical Sciences*, vol. 182, art. ID 105774, **DOI:10.1016/j.ijmecsci.2020.105774**.

[29] Si, H., Cao, L., Li, P.. (2020). Dynamic characteristics and stability prediction of steam turbine rotor based on mesh deformation. *Strojniški vestnik - Journal of Mechanical Engineering*, vol. 66, no. 3, p. 164-174, **DOI:10.5545/sv-jme.2019.6283**.

[30] Zhu, H., Chen, W., Zhu, R:, Gao, J., Liao, M. (2020). Study on the dynamic characteristics of a rotor bearing system with damping rings subjected to base vibration. *Journal of Vibration Engineering & Technologies*, vol. 8, p. 121-132, **DOI:10.1007/s42417-019-00082-8**.

[31] Zhang, Y., Yang, X., Zhang, W. (2020). Modeling and stability analysis of a flexible rotor based on the timoshenko beam theory. *Acta Mechanica Solida Sinica*, vol. 33, p. 281-293, **DOI:10.1007/s10338-019-00146-y**.